I&EC research
Industrial & Engineering Chemistry Research

pubs.acs.org/IECR

Article

Production of MOF Adsorbent Spheres and Comparison of Their Performance with Zeolite 13X in a Moving-Bed TSA Process for Postcombustion CO_2 Capture

Giorgia Mondino,* Aud I. Spjelkavik, Terje Didriksen, Shreenath Krishnamurthy, Ruth Elisabeth Stensrød, Carlos A. Grande, Lars O. Nord, and Richard Blom*

Cite This: *Ind. Eng. Chem. Res.* 2020, 59, 7198−7211

Read Online

ACCESS | Metrics & More | Article Recommendations | Supporting Information

ABSTRACT: Well-shaped 300−700 μm spheres of aggregated metal−organic framework CPO-27-Ni crystallites have been produced using a spray-granulation method with cross-bonded alginate as the binder. The spheres are suitable for use in a moving-bed temperature-swing adsorption (MBTSA) process for postcombustion CO_2 capture. The adsorption isotherm data of CO_2, N_2 ,and H_2O have been measured in the temperature intervalof 30−120 °C, and adsorption kinetics have been estimated from breakthrough measurements. The adsorption data together with the physical characteristics of the spheres (pore-size distribution and porosity) have been used to simulate the performance of a MBTSA process utilizing the CPO-27-Ni/alginate spheres as adsorbent and compared to similar simulations using Zeolite 13X spheres. Simulations have been carried out in a natural gas-fired power plant (NGCC) context. The process simulations indicate that the net electric efficiency of the NGCC plant with a MBTSA process utilizing the CPO-27-Ni/alginate spheres is similar to that of a MBTSA process utilizing Zeolite 13X adsorbent, 56.1% and 55.9%, respectively, which are slightly higher than the net efficiency of the benchmark case NGCC with a MEA-based solvent process of 54.7%.

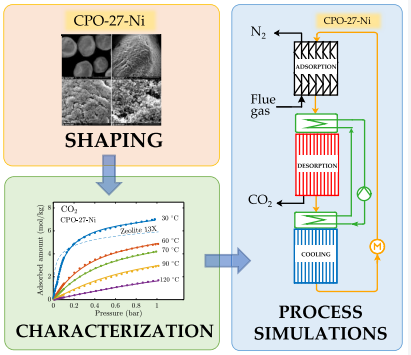

INTRODUCTION

Metal−organic frameworks (MOFs) are a class of microporous materials with large structural and chemical diversity and a high number of potential uses within adsorption-based technologies such as gas storage,[1−10] gas and liquid separation,[11−13] protection against toxic-industry compounds (TICs),[14] heat pumps and chillers,[15,16] water harvesting,[17] antimicrobial treatment,[18] catalysis,[19] and sensors.[20−22] Yet the use of MOFs is negligible commercially, partly due to upscaling and cost issues, and on the more technical side, one of the hindrances for further development is the lack of real testing of shaped MOFs under realistic conditions. Since most technologies require materials with a specific structure, either pellets, spheres, monoliths, or other, it is important that high yield methods for shaping MOFs are developed that maintain the good properties of the starting material but have a higher material density and a shape that gives optimal fluid transport throughout the material during the process. Having this, relevant data for the different applications can be obtained.

MOFs combine an inorganic atom, ion, or cluster with one or more multifunctional organic linkers to build up the porous framework. Some MOFs are only stable at relatively low temperatures and decompose readily when exposed to water, while others are stable under harsh conditions such as in boiling water over prolonged periods.[23] Furthermore, the physical stability of the MOF crystallites toward external pressures and elevated temperatures vary widely, and especially, MOFs having extremely high surface areas are the most sensitive and will collapse at relatively low pressures. Traditional methods for material shaping, such as extrusion and pelletization, involve the use of pressure, which often causes a significant reduction in specific surface area and porosity.[24−26] Therefore, in many cases, soft chemistry methods for MOF shaping are needed that give the wanted structures with the needed physical strength and at the same time maintain the porosity and surface area of the MOF.

When used in CO_2 capture technologies, the adsorbent material should be able to selectively adsorb CO_2 from the targeted gas mixture. In the case where the CO_2 is to be removed from a flue gas, either from power plants (coal or gas fired) or energy intensive industries (cement, steel, waste incinerators), the total pressure of the flue gas is often around 1 atm with 4−30 vol % CO_2, the rest being N_2, O_2, H_2O, and

Special Issue: Carbon Capture and Utilization

Received: November 21, 2019
Revised: March 28, 2020
Accepted: March 30, 2020
Published: March 30, 2020

https://dx.doi.org/10.1021/acs.iecr.9b06387
Ind. Eng. Chem. Res. 2020, 59, 7198−7211

varying amounts (most often in the ppm range) of SO_x, NO_x, and other impurities depending on the combustion source and flue gas cleaning. Disregarding the sulfur- and nitrogen-containing impurities, there are several MOFs that show promising performance for removal of CO_2 at low partial pressures in the presence of water vapor: the CPO-27/MOF-74/M_2(dobdc) (dobdc = 2,5-dioxidobenzene-1,4-dicarboxylate) family with either Mg or Ni as a metal component,[27] UTSA-16,[28] the SiFSIX family with either Cu or Zn as a metal component,[29] and last, but not least, the Diamin-appended mmen-Mg_2(dobpdc) (dobpdc = 4,4′-dioxidobiphenyl-3,3′-dicarboxylate) system,[30] all showing high selectivity for CO_2 over N_2, significant CO_2 capacity at around 10 kPa CO_2 pressure, and also reasonable stable cyclic performance in the presence of water vapor.[31−33]

We have recently developed a soft-chemical method to produce well-shaped MOF spheres based on the use of cross-bonded alginates.[34] With this method, we can produce MOF spheres containing 85−95 wt % MOF (dry basis) with negligible loss in specific surface area except the 10%−15% loss induced by the alginate in the spheres. The method is general but requires that the MOF is stable in water for the time needed to make the spheres, typically around 1 h.

Different processes need different sizes of the spheres. In the search for new promising adsorbent and processes for postcombustion CO_2 capture, we are building a lab-scale moving-bed temperature swing adsorption (MBTSA) unit.[35−38] Such a process will need adsorbent particles having good flowability and average diameters in the 0.3−1.0 mm range to avoid too long intraparticle diffusion pathways causing slow rate of adsorption. We believe spherically shaped particles will best fill these needs. We have recently presented the production and characterization of 2−3 mm spheres of CPO-27-Ni for fixed bed pressure-swing adsorption (PSA) applications.[32,39] In the present Article, we present the properties of CPO-27-Ni spheres and their production by the alginate method using a spray nozzle that gives the droplet size distribution in the range from 0.3 to 0.7 mm suitable for use in a MBTSA process. The method is based on adding the MOF powder to an aqueous alginate solution yielding a homogeneous slurry with low viscosity and the wanted alginate/MOF ratio allowing the slurry to be atomized by use of a suitable spray nozzle before entering a $CaCl_2$ solution. Divalent Ca^{2+} cross binds the alginate, fixating the droplet shape, yielding spherical alginate/MOF/H_2O beads which can be dried under mild conditions yielding dry alginate/MOF spheres. We present the physical characteristics of the spheres (size distribution, porosity, and density) and the adsorption properties relevant for postcombustion CO_2 capture: CO_2, N_2, and H_2O equilibrium isotherms and kinetic parameters estimated from breakthrough curves using the individual components. We have used the data to evaluate the performance of a MBTSA process for postcombustion CO_2 capture in an NGCC context. A comparison has also been done with recently published results obtained using Zeolite 13X spheres as the adsorbent.[38]

EXPERIMENTAL SECTION

Synthesis of CPO-27-Ni Powder. Around 100 g of batch CPO-27-Ni was produced in a 5.5 L autoclave using $Ni(CH_3COO)_2$ $4H_2O$ (99% from Aldrich) and 2,5-dihydroxyterephtalic acid (99.6% from Carbosynth) in an all-water synthesis as described in ref 32. Here, 224.0 g of Ni-acetate and 89.2 g of 2,5-dihydroxyterephtalic acid were separately suspended in 1.5 L of deionized water. The two suspensions were rapidly mixed together under continuous stirring before being introduced to the autoclave equipped with an impeller. The temperature was set to 110 °C, and the rotation speed of the impeller was set to 174 rpm. The reaction time was 71 h before the autoclave was cooled to ambient temperature overnight. After separating the product from the solvent by decantation and centrifugation, the crystalline powder was further washed three times with deionized water (approximately 1.5 L per wash lasting approximately 1 h) before storage as a wet sludge. The solid content of the sludge was estimated to be 24.2 wt % from measuring the mass before and after drying under vacuum overnight at 120 °C. The X-ray pattern (reported in the Supporting Information) is consistent with earlier CPO-27-Ni diagrams in ref 40.

Production of CPO-27-Ni Spheres. Here, 15.9 g of Alginate (Protanal LF10/60 from FMC) was dissolved in 1 L of deionized water and further stirred overnight to ensure a homogeneous solution. Then, 372.7 g of the wet CPO-27-Ni sludge (approximately 90.2 g of dry CPO-27-Ni) was added to the alginate/water solution. An additional 307.5 mL of deionized water was used to wash out the rest of the CPO-27-Ni sludge from the beaker. The slurry was then stirred overnight to ensure homogeneity. The setup used for spray-spheronizing CPO-27-Ni beads is shown in Figures S1 and S2 in the Supporting Information. Using a peristatic pump, the slurry is fed at a speed of 25 mL/min to a 0.5 mm spray nozzle using air at around 4.0 L/min as the atomizing agent. Then, 0.2 M $CaCl_2$ (98% from Aldrich) in deionized water was used as the gelation bath. After approximately 1 h, the spheres were removed from the gelation bath and washed. The washing was done by continuously flowing (approximately 3 L/h) tap water upward through a 1 L glass column with a glass filter keeping the spheres in place. This continuous washing took place for 21 h, and then, the spheres were collected and stored wet in a closed bottle. To find the optimal washing time, small samples of beads were removed from the washing setup after 45 min, 3 h, 21 h, and 45 h. BET analyses of the samples showed that 21 h were needed to reach a stable high specific surface area.

For comparison, a sample of the binderless Zeolite 13X spheres with sphere size distribution from 500 to 900 μm was received from CWK in Germany.

Adsorbent Characterization. *BET and Pore Characterization.* Specific surface areas were estimated from N_2 isotherms recorded at liquid nitrogen temperatures (77 K) using the BET formalism. Sample activation was typically carried out overnight at an external pretreatment unit (BELPREP II vac) at 120 °C under vacuum prior to a short (2 h) pretreatment at the BELSORP mini-instrument. The micropore volume was estimated using the t-plot method based on said N_2 isotherm measurements at 77 K, while larger pores were analyzed using a Hg porosimeter (Micromeritics AutoPore IV 9520) operating from 0.1 Pa to 414 MPa covering the pore diameter range from approximately 360 to 0.003 μm.

Thermal Stability (TG-DSC-MS). The thermal stability of the CPO-27-Ni precursor powder and the shaped beads were analyzed by using a TG-DSC-MS instrument (Netzsch STA 449 F1 instrument equipped with a QMS 403 C MS analyzer). Experiments were carried out using approximately 20 mg of material, a 2 °C/min heating rate, and an air flow of 50 mL/min. First, the samples were heated for 16 h in the air (50 mL/

https://dx.doi.org/10.1021/acs.iecr.9b06387
Ind. Eng. Chem. Res. 2020, 59, 7198−7211

min) at 90 °C to remove volatile components, and then, the samples were heated to 800 °C. Mass changes (TG) and heat transfer within the sample (DSC) as well as analyses of the kinds of volatile components leaving the sample during the process (by mass spectrometry, MS) were recorded. On the basis of the experiments, the thermal stability of the samples was evaluated.

Powder X-ray Diffraction. Powder X-ray diffraction patterns from 2θ = 5−60 of the MOF adsorbents were measured using a PANalytical EMPYREAN diffractometer equipped with a Cu source and Pixel 3D detector.

Scanning Electron Microscopy (SEM). Scanning electron microscopy pictures of the CPO-27-Ni spheres were collected on a FEI Nova NanoSEM 650 instrument.

Single Component Isotherm Measurements. Isotherms of pure CO_2, N_2, and H_2O were collected up to 1 bar (0.04 bar for H_2O) at different temperatures between 30 and 120 °C on a commercial volumetric BELSORP Max instrument (BEL, Japan). Sample activation was typically carried out overnight with an external pretreatment unit (BELPREP II vac) at 120 °C under vacuum prior to a short (2 h) pretreatment with the BELSORP Max instrument as part of the isotherm measurement procedure.

Adsorption Kinetics. Adsorption and desorption experiments were carried out using a dynamic column breakthrough apparatus. The schematic of the apparatus is shown in Figure 1. It consists of gas flow controllers to provide fixed flow rates,

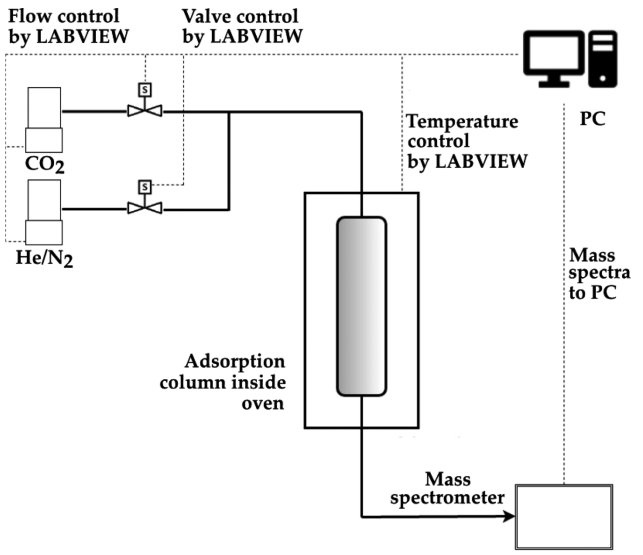

Figure 1. Schematic of the breakthrough setup.

an adsorption column housed in a temperature-controlled oven, and a mass spectrometer to detect the concentration downstream. Initially, the adsorbent column was regenerated under a helium/nitrogen purge of 100 mL/min overnight at 120 °C, and following that, the column was cooled to the experimental temperature of 50 °C. Once thermal equilibrium is reached, a step input in concentration was provided (6.5% CO_2 in He or N_2). The adsorption step was carried out with 17 mL/min of CO_2 and 261 mL/min of He or N_2 gas. After equilibrium was attained, desorption was carried out with the pure carrier gas. Experiments were carried out with two different particle sizes, namely, 300−500 and 500−700 μm. About 1.3 g of the smaller particles and 1.0 g of the larger particles were used in the experiments. Due to the difference in mass, the packed height for the two particle sizes were 7.3 and 4.6 cm, respectively. A thermocouple was also inserted into the packed bed to measure the temperature profile inside the adsorption column.

THEORETICAL BASIS

Modeling of Adsorption Isotherms. Equilibrium data of pure CO_2 and N_2 were fitted using the Virial isotherm model, given by[41,42]

$$P_i = \frac{q_i^*}{K_i}\exp[A_i q_i^* + B_i q_i^{*2} + C_i q_i^{*3}] \quad (1)$$

where subscript i indicates the adsorbate (CO_2 or N_2), of which p_i is the pressure, q_i the amount adsorbed, and K_i the Henry constant. The temperature dependence of the Virial coefficients A_i, B_i, and C_i was expressed by

$$A_i = A_{0,i} + \frac{A_{1,i}}{T_s};\ B_i = B_{0,i} + \frac{B_{1,i}}{T_s};\ C_i = C_{0,i} + \frac{C_{1,i}}{T_s} \quad (2)$$

while the Van't Hoff equation was used for the Henry constant

$$K_i = K_{\infty,i}\exp\left(\frac{\Delta H_i^0}{RT}\right) \quad (3)$$

where $K_{\infty,i}$ is the adsorption constant at infinite temperature, ΔH_i^0 the heat of adsorption at zero coverage, and R the universal gas constant.

The fitting of the experimental data to extract the model parameters was performed on Scilab 6.0.2[43] using the Nelder−Mead optimization routine for minimizing the square of residuals between the experimental data and predicted isotherms, in the whole temperature range simultaneously.

On the basis of the fitting parameters from pure gas measurements, multicomponent adsorption equilibrium can be predicted by applying the following extension of the Virial model[44]

$$P_i = \frac{q_i^*}{K_i}\exp\left[\sum_{j=1}^{N} A_{ij} q_j^* + \sum_{j=1}^{N}\sum_{k=1}^{N} B_{ijk} q_j^* q_k^* + \sum_{j=1}^{N}\sum_{k=1}^{N}\sum_{l=1}^{N} C_{ijkl} q_j^* q_k^* q_l^*\right] \quad (4)$$

where the mixing Virial coefficients are calculated as

$$A_{ij} = \frac{A_i + A_j}{2};\ B_{ijk} = \frac{B_i + B_j + B_k}{3};\ C_{ijkl} = \frac{C_i + C_j + C_k + C_l}{4} \quad (5)$$

Equations 4 and 5 were used in the MBTSA simulations to take into account competitive adsorption of N_2 and CO_2.

Modeling of Moving-Bed Temperature-Swing Adsorption (MBTSA) Process. On the basis of the measured equilibrium and kinetics properties, the use of the CPO-27-Ni spheres in a moving-bed temperature-swing adsorption process for CO_2 capture is evaluated via simulations.

The moving-bed system considered in this study, as schematically shown in Figure 2, consists of a series of units through which the adsorbent circulates while cyclically adsorbing and desorbing CO_2 by means of temperature swing. More specifically, the adsorption of CO_2 from the flue gas occurs within the top unit (adsorption section) where adsorbent and flue gas flow countercurrently to each other,

https://dx.doi.org/10.1021/acs.iecr.9b06387
Ind. Eng. Chem. Res. 2020, 59, 7198−7211

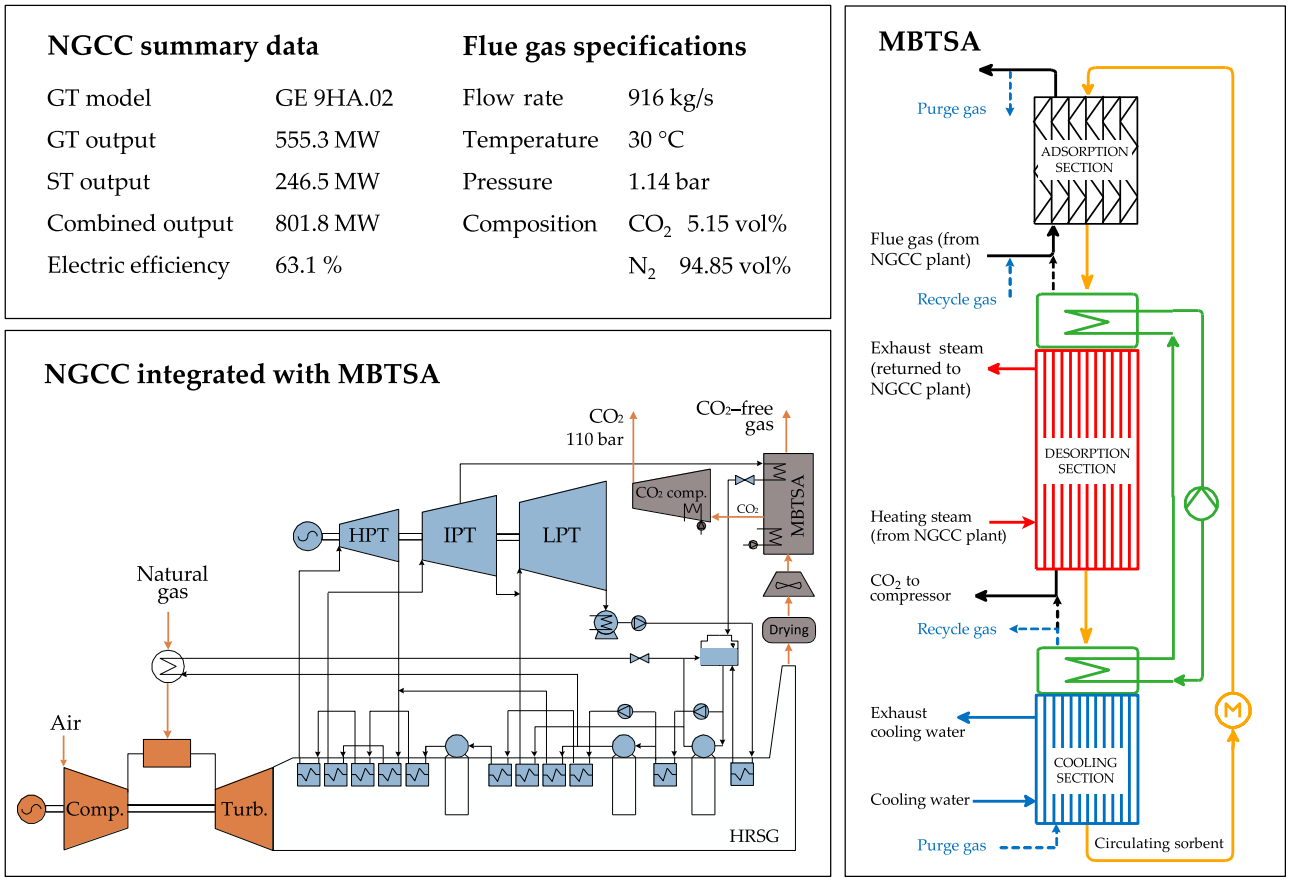

Figure 2. Specifications of the flue gas and reference NGCC power plant (top left), process flow diagram of the NGCC power plant with CO_2 capture (bottom left), and schematic diagram of MBTSA (right). The figure is a modified version of the one presented in ref 38.

with the adsorbent being fed from the top and the gas entering from the bottom.

The adsorbed CO_2 is then released and collected in a high CO_2 purity stream by increasing the temperature of the adsorbent as it passes through the desorption section, the latter being an indirect contact heat exchanger using steam as heating media. The cycle is then closed by indirectly cooling the regenerated adsorbent in the cooling section and returning it to the adsorption section for starting a new cycle. As shown in Figure 2, the system allows for a heat-integration scheme to reduce the external energy demand by recovering heat from the hot particles leaving the desorption section to be used for preheating the adsorbent before entering this section.

For process simulations, a detailed mathematical model of the MBTSA was implemented and solved in the gPROMS Model Builder.[45] Each section of the moving bed is described by a set of coupled partial differential equations distributed over the vertical coordinate, as described below (eqs 6–10).[36−38]

The profiles of the gas phase concentration along the section height are obtained from the mass balance in the gas phase

$$\varepsilon_c \frac{\partial C_i}{\partial t} = \varepsilon_c \frac{\partial}{\partial z}\left(D_z C_T \frac{\partial Y_i}{\partial z}\right) - \frac{\partial (uC_i)}{\partial z} - \frac{(1-\varepsilon_c-\xi)a' K_m}{\mathrm{Bi}/5+1}(C_i - C_{p,i}) \tag{6}$$

where t is time; z the position along the section height; C_i, $C_{p,i}$, and Y_i the concentration in the bulk gas, the concentration in the macropores, and the molar fraction, respectively, (with the index i being either CO_2 or N_2); ε_c the bed void fraction; ξ bed fraction occupied by the structured packing; D_z the axial dispersion; C_T the total concentration; u the gas velocity; a' the adsorbent particle specific area; K_m the film mass transfer coefficient; and Bi the Biot number.

Using the linear driving force (LDF) approximation to express the macropore mass transfer, the mass balance in the macropores is given by

$$\varepsilon_p \frac{\partial C_{p,i}}{\partial t} = \varepsilon_p \frac{15 D_{p,i}}{R_p^{\,2}} \frac{Bi_i}{5+Bi_i}(C_i - C_{p,i}) - \rho_p\left(\frac{\partial q_i}{\partial t} + v_s \frac{\partial q_i}{\partial z}\right) - v_s \frac{\partial C_{p,i}}{\partial z} \tag{7}$$

where R_p is the particle radius, $D_{p,i}$ the macropore diffusivity, ρ_p the particle density, Bi_i the Biot number of component i, q_i the concentration of component i in the adsorbed phase, and v_s the velocity of the adsorbent.

Similarly, by expressing the mass transfer rate in the solid phase with a LDF model, the adsorbent loading profiles are computed from the mass balance in the solid phase given by

$$\frac{\partial q_i}{\partial t} + v_s \frac{\partial q_i}{\partial z} = \frac{15 D_{c,i}}{r_c^{\,2}}(q_i^* - q_i) \tag{8}$$

where $D_{c,i}$ is the micropore diffusivity, $15D_c/r_c^2$ the adsorption rate of component i in the micropores, and q_i^* the adsorbed concentration of component i in equilibrium with the corresponding local concentration in the macropore ($C_{p,i}$). As previously mentioned, the adsorption equilibrium is described using the extension of the Virial isotherm model for multicomponent systems (eq 4).

https://dx.doi.org/10.1021/acs.iecr.9b06387
Ind. Eng. Chem. Res. 2020, 59, 7198−7211

Finally, the gas and the adsorbent temperatures (T and T_s) are predicted by solving the energy balances in the gas phase (eq 9) and the energy balance in the solid phase (eq 10), respectively.

$$\varepsilon_c C_T c_v \frac{\partial T}{\partial t} = \frac{\partial}{\partial z}\left(\lambda \frac{\partial T}{\partial z}\right) - u C_T c_p \frac{\partial T}{\partial z} + \varepsilon_c RT \sum \frac{\partial C}{\partial t} - (1 - \varepsilon_c - \xi) a' h_f (T - T_s) - \frac{4 h_{g,hx}}{D_h}(T - T_{hx}) \quad (9)$$

$$[(1 - \varepsilon_c - \xi)\rho_p c_{ps} + \xi \rho_{pk} c_{pk}]\left(\frac{\partial T_s}{\partial t} + v_s \frac{\partial T_s}{\partial z}\right) = \xi \frac{\partial}{\partial z}\left(\lambda_{pk} \frac{\partial T_s}{\partial z}\right) + (1 - \varepsilon_c - \xi) a' h_f (T - T_s) + (1 - \varepsilon_c - \xi)\rho_p \sum \left(-\Delta H_i \left[\frac{\partial q_i}{\partial t} + v_s \frac{\partial q_i}{\partial z}\right]\right) + (1 - \varepsilon_c \xi)\varepsilon_p R T_s \sum \left[\frac{\partial C_{p,i}}{\partial t} + v_s \frac{\partial C_{p,i}}{\partial z}\right] \quad (10)$$

In the previous equations, ΔH_i represents the heat of adsorption, h_f the film heat transfer coefficient between the gas and the solid, $h_{g,hx}$ the convective heat transfer coefficient between the gas and the wall, D_h the hydraulic diameter, T_{hx} the temperature of the heat transfer surface, c_v and c_p the gas specific heat capacities at constant volume and constant pressure, respectively, λ and λ_{pk} the heat axial dispersion coefficient of the gas and the packing, respectively, and R the universal gas constant.

The spatial derivatives of the equations above were discretized applying the centered finite difference method with second-order approximation. The number of discretization intervals was set to 400 for the adsorption and desorption sections, 100 for the preheating section, and 300 for the cooling section. As described in more details in a previous work,[37,38] the gPROMS composite model approach[46] was used to connect the individual sections of the MBTSA in a single flowsheet and solve simultaneously the corresponding model equations, given the appropriate boundary conditions. The dynamic simulations were performed until a steady state was reached, and all results presented here refer to the steady state solution.

Further details on the approach used for model implementation and the underlying model assumptions can be found elsewhere,[37,38] while additional equations and main correlations used for computing mass and heat transfer parameters are reported in the Supporting Information.

Integration of Capture Process with Power Plant. The application of the MBTSA capture process considered in the present study refers to a natural gas combined cycle (NGCC) power plant. The impact of the capture process on the power cycle efficiency was investigated via process simulations. For this purpose, a computational model of the NGCC opportunely modified to accommodate the CO_2 capture unit was used. The model, implemented in THERMOFLEX,[47] was developed in a previously published work[38] with the purpose of performing a detailed analysis of the energy use associated with the various CO_2 capture auxiliaries, as well as allowing a direct and consistent comparison with the benchmark amine-based technology. The main characteristics of the reference NGCC (without CO_2 capture) are given in Figure 2, together with the flue gas specifications used as input to the MBTSA simulations. It should be noted that the composition of the flue gas was simplified to a binary mixture of N_2 and CO_2 in order to reduce the computational time of the moving-bed simulations. Furthermore, due to the large amount of flue gas to be treated, the use of two MBTSA units was assumed. Figure 2 also presents a schematic layout of the simulated NGCC, showing the components that have been added to the reference NGCC to mimic the presence of the MBTSA. Besides the extraction of steam needed for sorbent regeneration (i.e., in the desorption section of the moving bed), the following components are included in the model: (i) a water circuit to provide cooling to the cooling section of the moving bed, (ii) a booster fan to overcome the pressure drops occurring in the adsorption section, (iii) a drying unit to dehydrate the flue gas upstream of the MBTSA, and (iv) an intercooled CO_2 compressor. The details on how the results from the MBTSA simulations were used as basis for the integration, providing the necessary inputs to the power plant simulations, is presented in ref 38.

RESULTS AND DISCUSSION

Adsorbent Properties. We have prepared CPO-27-Ni in an all-water synthesis at a 100 g scale yielding microcrystalline powder (Figure S3). Further, the washed powder was shaped by a spray-spheronization technique at productivities around 100 g/h yielding free-flowing well-shaped 300−700 μm spheres. Comparisons of the physical parameters of the CPO-27-Ni spheres with those of the reference Zeolite 13X sample are given in Table 1. The surface area of the CPO-27-Ni spheres is somewhat lower than that of the water washed precursor CPO-27-Ni powder (1250 m^2/g). The reduction in BET area is somewhat larger than expected from the amount of alginate in the spheres (15.0 wt % on dry basis). It should be noted that extensive washing of the spheres in a continuous flow of water over more than 20 h is needed to reach the BET area noted in Table 1. The long washing time needed is most likely because removal of unreacted precursors stemming both from the MOF synthesis and from the shaping takes a longer time for the beads due to the longer diffusion pathways compared to the micron-sized CPO-27-Ni precursor crystalline powder.

Table 1. Physical Properties of CPO-27-Ni and Zeolite 13X Spheres Used in This Study

	CPO-27-Ni	Zeolite 13X
Sphere diameter distribution (μm)	500−700	500−900
Specific BET area (m^2/g)	960	740
Micropore volume (mL/g)[a]	0.37	0.32
Mesopore volume (mL/g)[b]	0.00	0.09
Macropore volume (mL/g)[b]	0.52	0.28
Sphere density (g/mL)	0.739	0.924
Sphere porosity (%)	38	34

[a]From N_2 adsorption at 77 K using the t-plot method. [b]From Hg-porosimetry accumulated Hg intrusion at 414 MPa. [c]Sphere density = (specific crystal volume + mesopore and macropore volume)$^{-1}$. [d]Sphere porosity = mesopore and macropore volume × sphere density.

Figure 3 shows the SEM pictures of the CPO-27-Ni spheres at different magnifications. The sphericity is not perfect but reflects the droplet shape and gelation kinetics of the process.

https://dx.doi.org/10.1021/acs.iecr.9b06387
Ind. Eng. Chem. Res. 2020, 59, 7198−7211

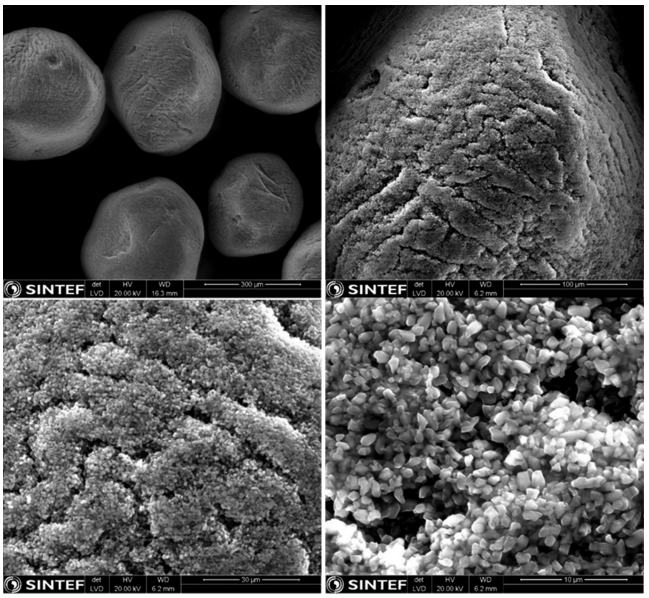

Figure 3. SEM pictures at increasing magnification of the CPO-27-Ni spheres made for MBTSA application.

When we go closer into the sphere surface, we see clearly the individual micron-sized CPO-27-Ni crystallites, but the alginate network that keeps the MOF crystals together stays invisible due to the high acceleration voltage used in the analysis. The CPO-27-Ni crystals are densely packed into aggregates with "ravines" (1−5 μm wide) between the aggregates that might be voids of alginate-rich areas. The

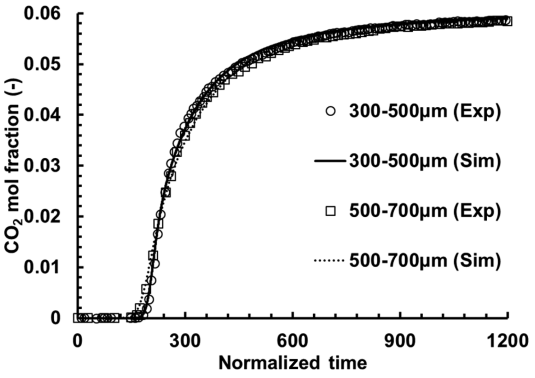

Figure 5. CO_2 breakthrough profiles for different pellet sizes at 50 °C. The x axis is normalized time to show the effect of particle size.

Hg-intrusion analysis shows two domains of filling (Figure S4 and S5, Supporting Information). First, a filling at around 100 μm is most probably filling of the voids between the spheres. No filling is observed between 1 and 10 μm, indicating that the "ravines" observed in the SEM pictures are not voids but more probably cross-bonded alginat-rich areas with no porosity. Lastly, there is filling due to the presence of macropores with the average pore diameter around 120 nm, consistent with the voids between the submicron-sized crystals observed by SEM. Since the crystal size distribution is narrow, also the macropore size distribution is quite narrow.

The Hg-intrusion curve for Zeolite 13X shows a similar pattern: First, a filling of the voids between the spheres, then a macropore filling at around 120 nm, but for this material there

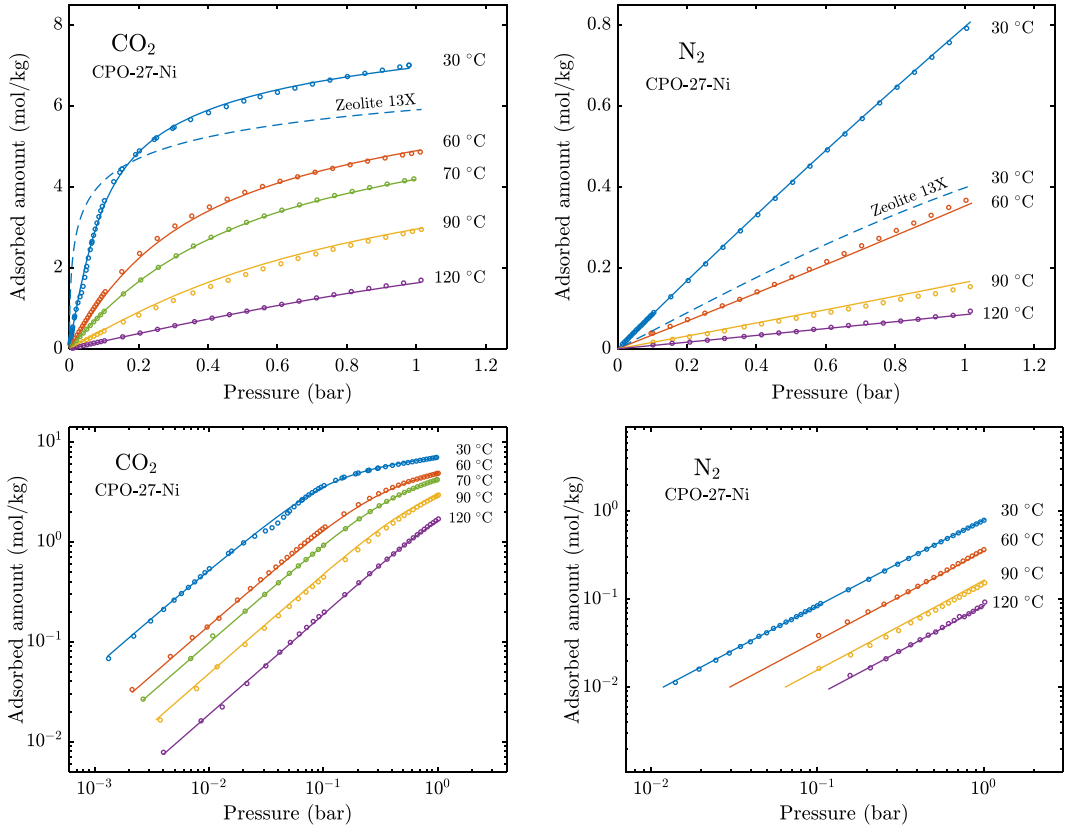

Figure 4. Adsorption isotherms of CO_2 and N_2 on CPO-27-Ni spheres in linear (top) and logarithmic scales (bottom).

https://dx.doi.org/10.1021/acs.iecr.9b06387
Ind. Eng. Chem. Res. 2020, 59, 7198−7211

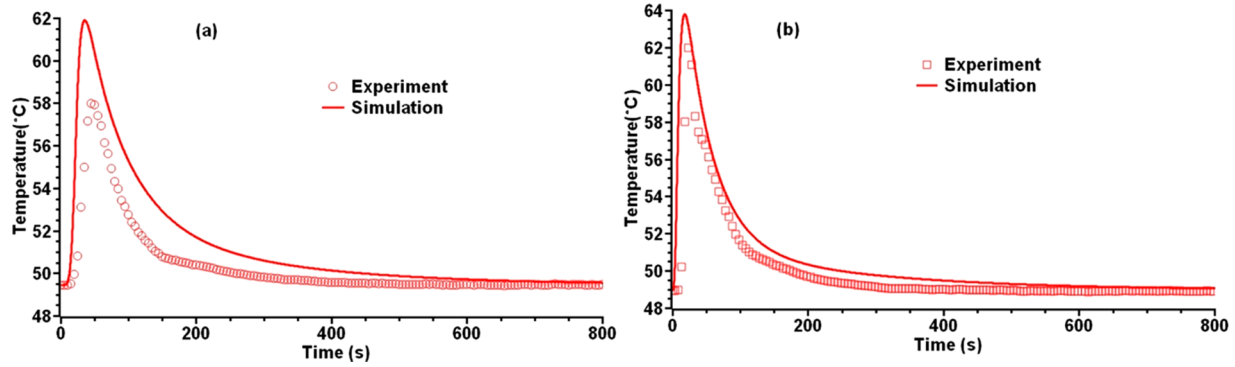

Figure 6. Temperature profile inside the column packed with (a) 300−500 and (b) 500−700 μm CPO-27-Ni spheres.

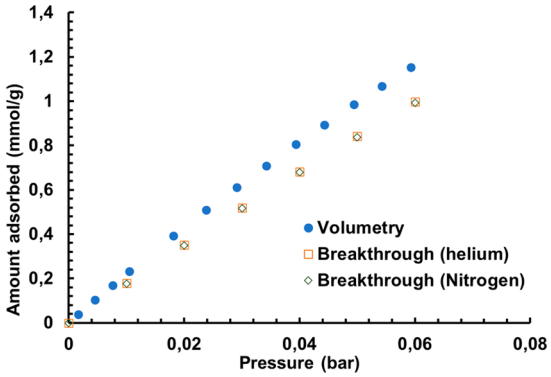

Figure 7. Adsorption capacity of CO_2 on CPO-27-Ni spheres obtained from breakthrough experiments performed at 50 °C, using helium (red box) and nitrogen (green diamond) as carrier gases. Comparison with values extrapolated from volumetric isotherm measurements.

is also a small mesopore volume of around 0.09 mL/g at around 4−5 nm pore diameter.

The porosities of the CPO-27-Ni and Zeolite 13X spheres are 38% and 34%, respectively, based on mesopore and macropore volumes of 0.52 and 0.37 mL/g, respectively, from the Hg-porosimetry analysis. Sphere densities are estimated to 0.74 and 0.92 g/mL, respectively. The differences in sphere densities reflect the difference in the crystallographic densities of the precursor CPO-27-Ni and Zeolite 13X crystals, 1.2 and 1.404 g/mL, respectively,[48,49] and also that the macropore volume of the spray-spheronized CPO-27-Ni adsorbent is higher than that of the Zeolite 13X spheres. We believe the extra porosity is a consequence of the spray method used and that lower porosities might be achieved using other droplet-forming methods and/or alginate types or contents. Minimizing the sphere mesoporosity and macroporosity is important to further increase the volumetric CO_2 capacity of the adsorbent and consequently reduce the size of the MBTSA process. The crystalline densities should be regarded as the maximum sphere densities achievable of the respective materials that cannot be exceeded without partial destruction of the crystal lattice.

Table 3. Main Design Parameters and Operating Conditions Used in Simulations of the MBTSA Process[a]

	CPO-27-Ni	Zeolite 13X
Height of adsorption section (m)	3.5	1.5
Cross-sectional area in adsorption section (m^2)	254.5	254.5
Column void fraction in adsorption section (−)	0.8	0.8
Cross-sectional area in other sections (m^2)	78.5	78.5
Column void fraction in adsorption section (−)	0.6	0.6
Height of preheating section (m)	3.0	2.0
Height of desorption section (m)	6.0	9.0
Height of cooling section (m)	10	12
Adsorbent residence time/cycle time (min)	26	45
CO_2 extraction pressure (bar)	0.97	0.97
Amount of circulating sorbent (kg/s)	350	245
Regeneration temperature (°C)	132	207

[a]Values referred to a single MBTSA unit.

The TG-DSC traces of CPO-27-Ni precursor powder and CPO-27-Ni/alginate beads are indistinguishable (Figures S6 and S7). However, we know from previously published work with MOF/alginate spheres that the alginate itself starts decomposing at around 135 °C.[50]

Adsorption Equilibrium. The adsorption isotherms of CO_2 and N_2 measured on the CPO-27-Ni spheres are shown in Figure 4, while H_2O isotherms are given in Figure S8 in the Supporting Information. In Figure 4, the isotherms at 30 °C are compared with the corresponding Zeolite 13X isotherms published in a previous work.[38] Although the highest measured CO_2 uptake (recorded at 100 kPa and 30 °C) of the MOF is higher than on Zeolite 13X, the CO_2 capacity of CPO-27-Ni is significantly lower when compared at low partial pressures relevant for postcombustion capture applications where the adsorption of CO_2 is typically carried out at low temperature and low CO_2 partial pressure. Further the isotherm of CO_2 in CPO-27-Ni is less steep than that of Zeolite 13X. On the other hand, CPO-27-Ni adsorbs significantly less CO_2 than Zeolite

Table 2. Summary of Kinetics Experiments on CPO-27-Ni Spheres

Conditions						
Spheres size (μm)	Carrier gas	$D_{molecular}$ ($\times 10^{-5}$ m^2/s)	$D_{Knudsen}$ ($\times 10^{-5}$ m^2/s)	K	k_{LDF} (s^{-1})	Tortuosity
300−500	He	7.0	2.2	301	4.41	3.3
300−500	N_2	1.9	2.2	293	2.66	3.4
500−700	He	7.0	2.2	500	1.56	2.8

https://dx.doi.org/10.1021/acs.iecr.9b06387
Ind. Eng. Chem. Res. 2020, 59, 7198−7211

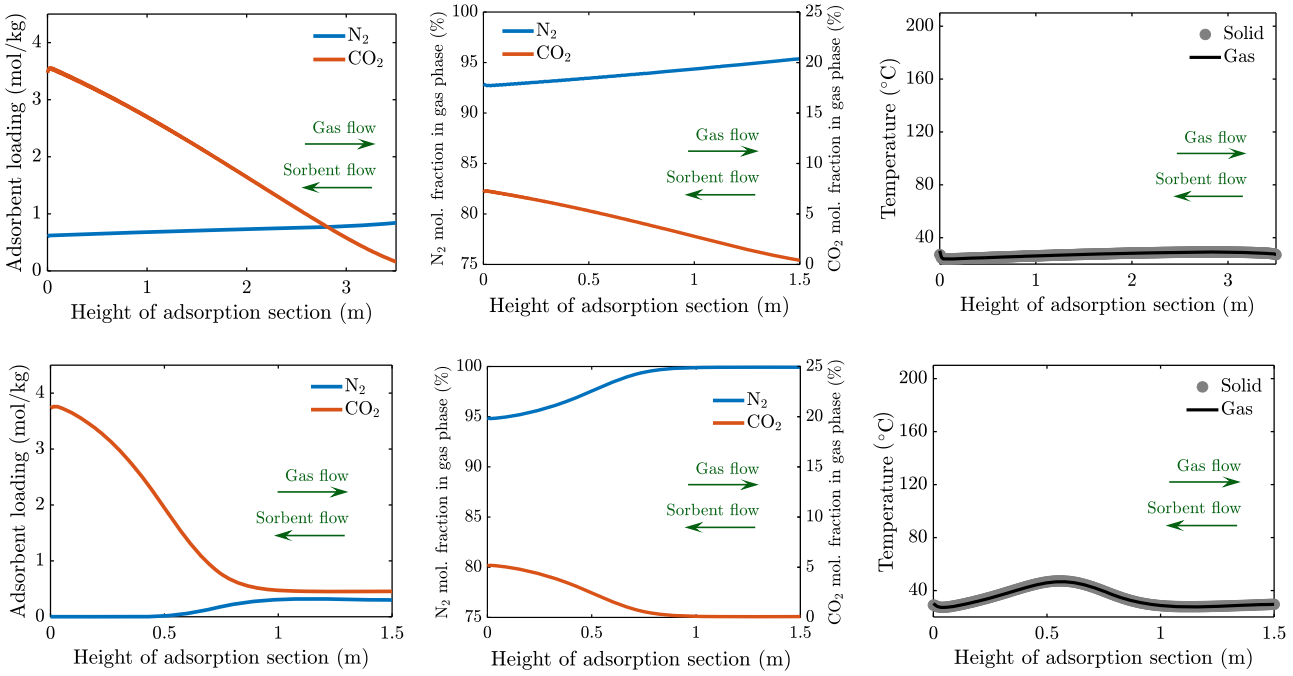

Figure 8. Adsorbent loading, molar fractions, and temperature profiles along the height of the adsorption section of the moving bed using CPO-27-Ni spheres (top plots) and Zeolite 13X (bottom plots). The flue gas flows countercurrently to the adsorbent: position zero corresponds to the bottom of the section, i.e., flue gas inlet and adsorbent outlet.

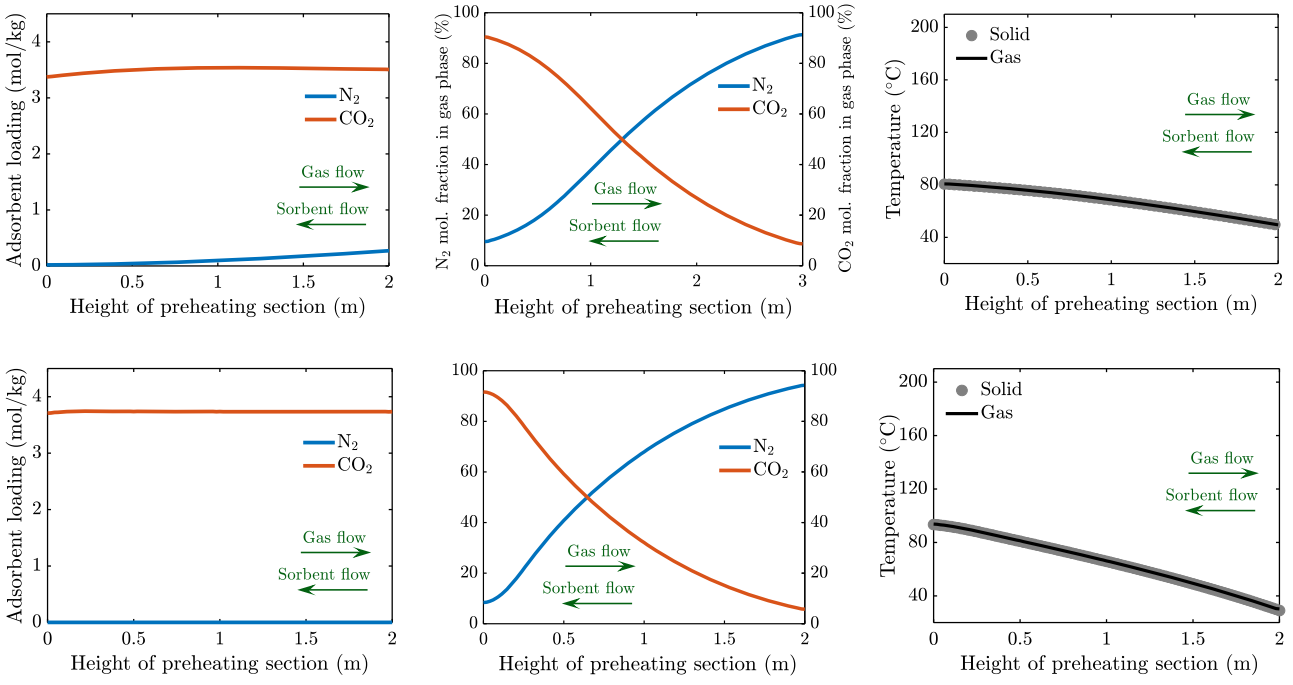

Figure 9. Adsorbent loading, molar fractions, and temperature profiles along the preheating section of the moving bed using CPO-27-Ni (top plots) and Zeolite 13X (bottom plots). Position zero corresponds to outlet of the adsorbent (bottom of the section).

13X also at high temperature and close to atmospheric pressure, i.e., at desorption (regeneration) conditions in a temperature swing capture process, which means that for a given regeneration temperature a higher level of regeneration can be achieved with the MOF. Figure 4 also shows the results of the fitting with the Virial model obtained by simultaneous nonlinear regression of the data in the whole temperature range. The fitted parameters are reported in the Supporting Information together with the corresponding values of the Zeolite 13X.[38] The obtained heat of adsorption of CO_2 is lower for CPO-27-Ni (37.4 kJ/mol) than for Zeolite 13X (44.8 kJ/mol), which is beneficial in terms of limiting the energy requirement of the capture process. The estimated heat of adsorption for the CPO-27-Ni spheres is close to previously reported values of 38−39 kJ/mol for powder samples.[27,51]

Adsorption Kinetics. Figures 5 and 6 show the CO_2 adsorption breakthrough trace and the temperature profiles with different pellet sizes using helium as the carrier gas. The

https://dx.doi.org/10.1021/acs.iecr.9b06387
Ind. Eng. Chem. Res. 2020, 59, 7198−7211

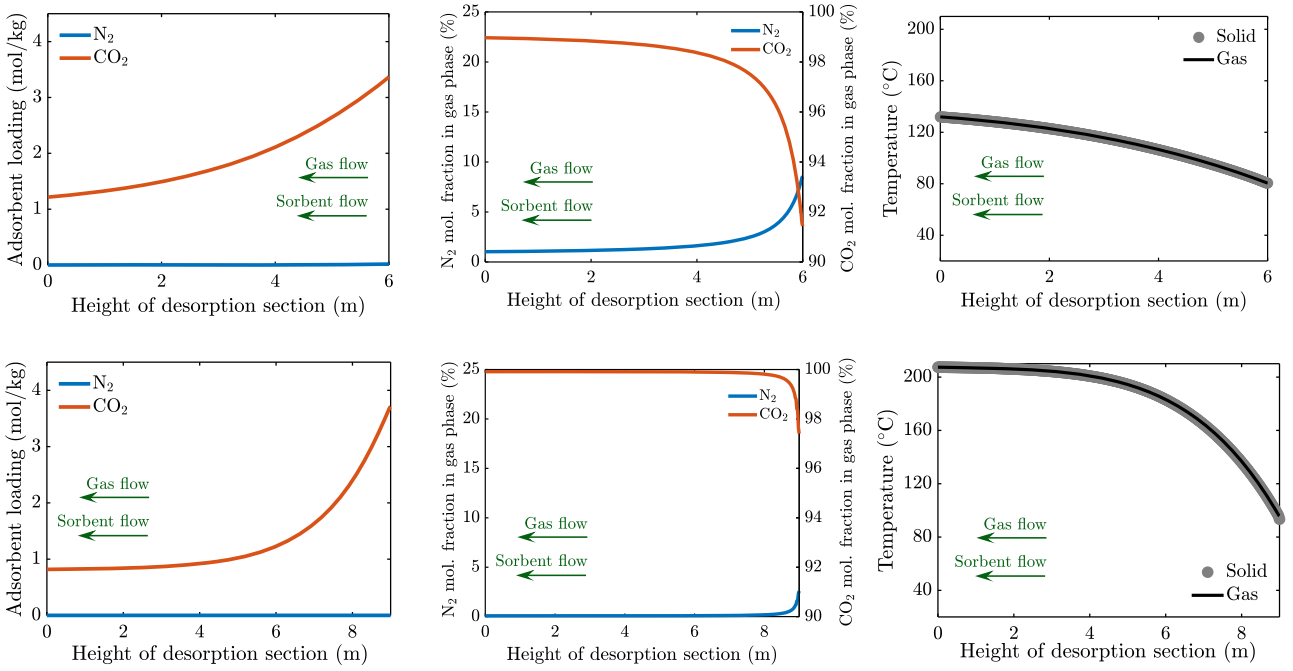

Figure 10. Adsorbent loading, molar fractions, and temperature profiles along the desorption section of the moving bed (top plots) and Zeolite 13X (bottom plots). The flue gas flows countercurrently to the adsorbent: Position zero corresponds to the bottom of the section, i.e., CO_2 extraction point, and sorbent outlet.

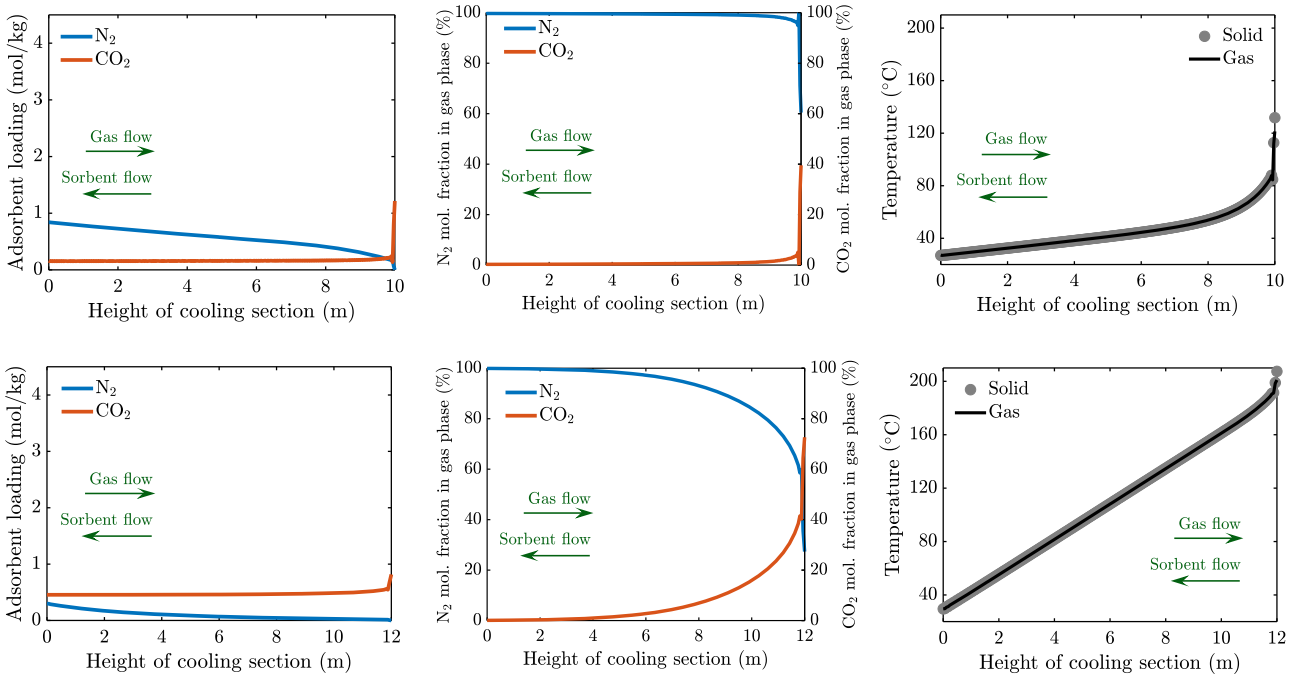

Figure 11. Adsorbent loading, molar fractions, and temperature profiles along the cooling section of the moving bed using CPO-27-Ni spheres (top plots) and Zeolite 13X (bottom plots). Position zero corresponds to the bottom of the section, i.e., inlet of recirculation gas, and sorbent outlet.

CO_2 trace for the larger particles is more spread out than that of the smaller particles indicating that the mass transfer is a function of the particle size. This is consistent with earlier data concluding that the adsorption of CO_2 in CPO-27-Ni is governed by diffusion in the macropores.[39,52,53]

Using the desorption trace, a mass balance was performed to obtain the adsorption isotherm up to 6 kPa as described by Brandani et al.[54] As helium gas is considered inert, the capacity curve obtained is equivalent to a single component isotherm. The capacity value obtained at 6 kPa CO_2 pressure was 1 mmol/g. This is about 15% less than the "extrapolated" value from single component isotherms from the volumetric measurements as seen in Figure 7. This difference can be attributed to the different regeneration conditions used in the two experiments. The competitive isotherm of CO_2 in the presence of nitrogen showed that at 50 °C, the nitrogen does not affect the adsorption of CO_2. This may not be the case at low temperatures, where the competition could be stronger.

https://dx.doi.org/10.1021/acs.iecr.9b06387
Ind. Eng. Chem. Res. 2020, 59, 7198−7211

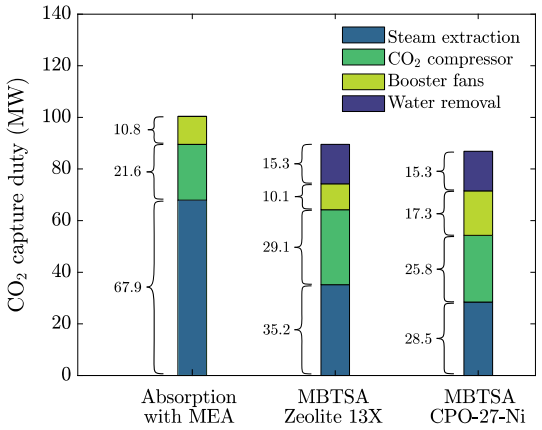

Figure 12. Individual contributions to the overall capture duty. Comparison of the MBTSA process with CPO-27-Ni, MBTSA with Zeolite 13X, and the amine-based process.

In order to extract the kinetic parameters from the breakthrough curves, a nonisothermal, nonisobaric 1D model was then used to fit the experimental profiles.[55] The model equations are described in the Supporting Information. The residual between the simulated and experimental adsorption breakthrough profiles was minimized by fitting the isotherm parameters, the LDF coefficient, and the heat transfer coefficient values.

In the first step, the helium experiment was analyzed. For nonadsorbing helium, the affinity coefficient and heat of adsorption values were taken as zero, and the LDF coefficient was kept as 1000 s^{-1}. The fitting of the breakthrough experiments was carried out in MATLAB.[56] The results from the modeling are shown in Figures 5 and 6 and summarized in Table 2. In general, there is a good agreement between the experimental and simulated profiles.

The ratio of the LDF coefficient values for the smaller and larger pellets was found to be 2.8, which is slightly higher than the ratio of the square of the average particle diameters (2.25). With respect to the different carrier gas, the ratios of the estimated LDF constants were similar to the ratio of the respective macropore diffusivity values. In these experiments, the total pressure was constant and hence, for the macropore diffusivity is a combination of Knudsen and molecular diffusivities and given by

$$\frac{1}{D_{\text{macro}}} = \frac{1}{D_{\text{molecular}}} + \frac{1}{D_{\text{Knudsen}}} \tag{11}$$

The molecular and the Knudsen diffusivity values were calculated by the correlations given in eqs 12 and 13. The 9/13 in the Knudsen diffusivity value is the Derjaguin correction factor.[57] The breakthrough experiments were coupled with independent mercury intrusion experiments which gave the porosity and pore radius. The LDF correlation was then rearranged to extract the values of the tortuosity which are provided in the same table. For the smaller pellets, the tortuosity value was found to be 1.8 ± 0.1, and for the large pellets, it was 1.4 ± 0.1.

$$D_{\text{molecular}} = \frac{0.001858T^{1.5}}{P\sigma^2\Omega}\sqrt{\frac{1}{M1} + \frac{1}{M2}} \tag{12}$$

$$D_{\text{Knudsen}} = \frac{9}{13}(0.97)r_{\text{Pore}}\sqrt{\frac{T}{M}} \tag{13}$$

Simulations of MBTSA for CO_2 Capture Using CPO-27-Ni Spheres and Comparison with Zeolite 13X. As basis for the design of the MBTSA with CPO-27-Ni, the process developed in a previous work using Zeolite 13X was taken as the initial configuration. A series of simulations was then performed by iteratively adjusting certain design parameters until desired process performances were achieved. In this respect, a minimum of 95% CO_2 purity and 90% CO_2 capture rate were set as targets. The list of design parameters that were modified and their final values used in the simulations presented here are reported in Table 3, together with the corresponding values of the original parameters from the zeolite case.

In terms of constraints to be taken into account when adjusting the operating conditions, a major difference between the zeolite and the MOF cases was on the choice of the regeneration temperature; while no limitation was imposed in the zeolite study, a temperature of 133 °C was set as the maximum desorption temperature for the CPO-27-Ni case in order to avoid potential degradation of the adsorbent. As suggested by the isotherm plots in Figure 4, this means that the adsorbent will still contain a significant amount of CO_2 adsorbed (above 1 mol/kg) when leaving the desorption section. In other words, only part of the captured CO_2 will be recovered as a result of a temperature increase occurring within

Table 4. Main Simulation Results of MBTSA with CPO-27-Ni and Integration of Capture Process with NGCC Power Plant[a]

	NGCC without CO_2 capture	NGCC with amine-based process (MEA)	NGCC with MBTSA, Zeolite 13X	NGCC with MBTSA, CPO-27-Ni
CO_2 purity (%)		99.9	95.8	98.9
CO_2 capture efficiency (%)		95.0	98.2	92.6
Heat input to capture unit (MW_{th})		266	101	125
Specific heat input ($MJ/kg_{CO2captured}$)		3.95	1.42	1.89
NGCC emissions (t_{CO2}/h)	253	11.2	4.6	18.8
CO_2 captured (kg/h)	–	242	249	240
NGCC specific emissions (kg/MWh)	316	15	6	24
NGCC gross power output (MW_{el})	802	734	767	773
GT gross electric power output (MW_{el})	555	555	555	555
ST gross electric power output (MW_{el})	246	179	211	218
CO_2 capture auxiliaries (MW)		37.5	54.7	60.1
NGCC net electric efficiency (%)	**63.1**	**54.7**	**55.9**	**56.1**

[a]Comparison with Zeolite 13X study[38] and capture with amine-based capture process.[38]

https://dx.doi.org/10.1021/acs.iecr.9b06387
Ind. Eng. Chem. Res. 2020, 59, 7198−7211

the desorption section. However, the remaining CO_2 can be recovered by further purging the adsorbent while traversing the subsequent cooling section. For this purpose, a small fraction (approximately 5 wt %) of the CO_2-free product gas from the adsorption section is recirculated to the cooling section, where it flows countercurrently to the adsorbent inducing further desorption of CO_2. The flow of recirculated gas through the cooling section also serves to maintain the pressure inside the column close to atmospheric pressure, as the cooling of the adsorbent would otherwise promote adsorption of the surrounding gas, and thus a decrease in pressure in the bulk phase. As a result of this recirculation through the cooling section, a small gas stream (approximately 7 wt % of the feed gas) containing a certain amount of CO_2 will be released from the top of the cooling section. As shown in Figure 2 (dashed blue stream lines), the released gas is then recycled and mixed with the flue gas feeding the adsorption section, with the purpose of improving the recovery of CO_2, by simultaneously increasing the CO_2 partial pressure in the feed gas. For simplicity, it is assumed that the recycled gas is cooled to the feed gas temperature before mixing. A similar strategy was adopted in the zeolite case, with the difference that the resulting product gas from the cooling (shown in dashed black line in Figure 2) section was directly mixed with the CO_2 product obtained from the desorption section, rather than being mixed with the feed gas.

The simulation results in terms of concentration and temperature profiles along the height of each moving-bed section are shown in Figure 8−11 and compared with the profiles obtained using Zeolite 13X. One of the main differences between the two cases concerns the shape of the concentration profiles in the adsorption section. As CPO-27-Ni presents a more spread profile, it was necessary to increase the length of the adsorption to 3.5 m (versus the original 1.5 m of the zeolite case), leading to higher pressure drops. The reason for this is related to the difference in the CO_2 adsorption isotherms of the two adsorbents at the feed gas conditions, which are steeper in the zeolite. Another difference that can be observed by looking at Figure 8 is the higher amount of N_2 coadsorbing with CO_2 on CPO-27-Ni, as result of the lower equilibrium selectivity of CPO-27-Ni compared to Zeolite 13X. However, this does not affect the purity of the CO_2 product (which is collected from the desorption section), as the N_2 desorption occurs within the preheating section (Figure 9). Here, the adsorbent undergoes a first increase in temperature, which induces a shift in adsorption equilibrium: Most of the adsorbed N_2 is released to the gas phase with the accompanying gas being removed from the top, while simultaneously, the CO_2 concentration in the gas phase increases without a significant change in the adsorbed concentration. In a similar way as for the gas recovered from the cooling section, the gas released from the preheating section is recycled to the feed gas (shown as dashed black line in Figure 2), being approximately 1 wt % of the total flow rate. The majority of CO_2 is then desorbed as a result of further heating of the adsorbent occurring in the desorption section (Figure 10). By setting a mild vacuum (0.97 bar) as evacuation pressure, the released gas is collected at the bottom, where high CO_2 purity is achieved. Lastly, adsorbent cooling is carried out in the cooling section (Figure 11), where a small stream of nearly pure N_2 recirculated from the adsorption section is used as purge gas to further regenerate the adsorbent from the remaining CO_2. As previously mentioned, the fraction of recirculated gas was approximately 5% of the total CO_2-free gas leaving the adsorption section.

As shown in Figures 8−11 and reported in Table 3, the advantage of the zeolite of having a shorter adsorption section is offset by the need for longer cooling and desorption sections, due to their higher regeneration temperature. In fact, with respect to sorbent inventory, the process using zeolite is outperformed by CPO-27-Ni: despite circulating a lower amount of material in terms of kg/s, the total amount of adsorbent required (i.e., the amount of adsorbent that is processed in one cycle) is 43% higher due to the much longer residence time of the zeolite.

Energetic Performance of Capture Process and Results of Power Plant Integration. On the basis of the results obtained with the MBTSA simulations, the amount of thermal energy required for sorbent regeneration was computed and used as input to the NGCC model simulations. The results of the power plant integration are summarized in Figure 12 and Table 4, together with a comparison with the reference NGCC plant (without capture), the benchmark amine-based process, and the reference moving-bed process using zeolite.

Very similar performances are obtained for the two MBTSA processes (Zeolite 13X and CPO-27-Ni) in terms of overall power cycle efficiency, causing approximately a 7%-point reduction in net electric efficiency, compared to an 8%-point capture penalty of the amine-based process. As shown graphically in Figure 12, one of the main differences between the moving-bed and amine-based systems is the need for drying the flue gas prior to the capture process when using solid sorbents, with the energy penalty associated with the drying process. Another factor playing in favor of the MEA process is the slightly higher pressure at which CO_2 is separated, which implies lower energy consumption by the CO_2 compressor. On the other hand, the MBTSA processes present a significantly lower heat demand for sorbent regeneration and hence a lower power loss associated with the steam extraction.

When comparing the zeolite-based process with the MOF-based process, the higher energy penalty due to the pressure drops in the CPO-27-Ni system is compensated by the lower reduction in power output associated with steam bleeding. In fact, despite requiring a slightly higher amount of energy for sorbent regeneration (both in terms of total heat input and specific heat per kg of CO_2 captured), CPO-27-Ni allows extraction of steam at lower pressure, which is beneficial for the steam cycle performance. Details on the steam extraction conditions and flow rates can be found in the Supporting Information.

■ CONCLUSIONS

We have prepared CPO-27-Ni/alginate spheres suitable for use in a moving-bed temperature-swing adsorption (MBTSA) process for postcombustion CO_2 capture. The shaped spheres maintain most of the CO_2 capacity of the CPO-27-Ni precursor powder but have better flow characteristics needed to avoid clogging in a MBTSA reactor. The MOF spheres have been compared with Zeolite 13X spheres of similar size. The two adsorbents have similar CO_2 capacities in mmol/g units, but the CPO-27-Ni/alginate spheres have lower volumetric CO_2 capacity due to the intrinsic lower crystallographic density of CPO-27-Ni compared to Zeolite 13X and to the larger macropore volume of the former because of the shaping

https://dx.doi.org/10.1021/acs.iecr.9b06387
Ind. Eng. Chem. Res. 2020, 59, 7198−7211

method used. Despite this difference, simulation of the two adsorbents in a MBTSA process for capturing CO_2 from an NGCC power plant indicate that the CPO-27-Ni spheres have lower energy requirements compared to Zeolite 13X, the main reason being a lower temperature needed for regeneration. Due to the high hydrophilicity of both adsorbents, a drying step of the flue gas is needed before the CO_2 capture process. Despite this extra process, the simulations show that the MBTSA process utilizing either adsorbent perform slightly better than a solvent-based MEA process in terms of energy requirements.

Further improving the shaping process used for CPO-27-Ni, especially minimizing the macropore volume of the spheres and thus increasing their volumetric CO_2 uptake, will further improve the performance of the MBTSA process. In particular, this will reduce the process footprint which is one of the major challenges with adsorbent-based processes.

■ ASSOCIATED CONTENT

Supporting Information

The Supporting Information is available free of charge at https://pubs.acs.org/doi/10.1021/acs.iecr.9b06387.

Setup used for MOF shaping; details on X-ray diffraction; Hg-intrusion and TG-DSC-MS analyses; tabulated data of CO_2, N_2, and H_2O isotherms; water isotherms plots; model equations used for modeling breakthrough curves; and additional equations used in the MBTSA simulations (PDF)

■ AUTHOR INFORMATION

Corresponding Authors

Giorgia Mondino − *Department of Energy and Process Engineering, NTNU − Norwegian University of Science and Technology, Trondheim, Norway*; Email: giorgia.mondino@ntnu.no

Richard Blom − *SINTEF Industry, 0314 Oslo, Norway*; orcid.org/0000-0001-8675-0774; Email: richard.blom@sintef.no

Authors

Aud I. Spjelkavik − *SINTEF Industry, 0314 Oslo, Norway*

Terje Didriksen − *SINTEF Industry, 0314 Oslo, Norway*

Shreenath Krishnamurthy − *SINTEF Industry, 0314 Oslo, Norway*; orcid.org/0000-0002-9584-6804

Ruth Elisabeth Stensrød − *SINTEF Industry, 0314 Oslo, Norway*

Carlos A. Grande − *SINTEF Industry, 0314 Oslo, Norway*; orcid.org/0000-0002-9558-5413

Lars O. Nord − *Department of Energy and Process Engineering, NTNU − Norwegian University of Science and Technology, Trondheim, Norway*

Complete contact information is available at: https://pubs.acs.org/10.1021/acs.iecr.9b06387

Author Contributions

The manuscript was written through contributions of all authors. All authors have given approval to the final version of the manuscript.

Funding

We acknowledge financial support from the CLIMIT program of the Norwegian Research Council for funding the EDeMoTeC project (Grant 267873).

Notes

The authors declare no competing financial interest.

■ ACKNOWLEDGMENTS

We want to thank Martin F. Sunding at SINTEF Materials Physics for recording the SEM pictures.

■ ABBREVIATIONS

CCR2 = CC chemokine receptor 2
CCL2 = CC chemokine ligand 2
CCR5 = CC chemokine receptor 5
TLC = thin layer chromatography
TG-DSC-MS = thermogravimetry and differential scanning calorimetry coupled with mass spectroscopy
GT = gas turbine
ST = steam turbine

■ NOMENCLATURE

A_i = first Virial coefficient of component i, kg mol^{-1}
a' = specific area of adsorbent particle, m^2 m^{-3}
B_i = second Virial coefficient of component i, kg mol^{-1}
Bi_i = Biot number of component i
C_i = third Virial coefficient of component i, kg mol^{-1}
C_i = concentration of component i in bulk gas phase, mol m^{-3}
$C_{p,i}$ = concentration of component i in the macropores, mol m^{-3}
c_p = molar specific heat of gas mixture at constant pressure, J mol^{-1}K^{-1}
$c_{p,s}$ = specific heat of solid phase, J kg^{-1}K^{-1}
C_T = total gas concentration in bulk phase, mol m^{-3}
c_v = molar specific heat of gas mixture at constant volume, J mol^{-1} K^{-1}
$D_{c,i}$ = micropores/crystals diffusivity of component i, m^2 s^{-1}
D_h = hydraulic diameter, m
D_{Knudsen} = Knudsen diffusivity, m^2 s^{-1}
D_{macro} = diffusivity in macropores, m^2 s^{-1}
$D_{\text{molecular}}$ = molecular diffusivity, m^2 s^{-1}
$D_{p,i}$ = macropore diffusivity of component i, m^2 s^{-1}
D_z = axial dispersion coefficient, m^2 s^{-1}
K_i = equilibrium constant of component i, mol kg^{-1} bar^{-1}
K_{eq}^{∞} = equilibrium constant at infinite temperature, mol kg^{-1} bar^{-1}
h_f = film heat transfer coefficient between the gas and the particle, J s^{-1} m^{-2} K^{-1}
$h_{g,hx}$ = film heat transfer coefficient between the gas and the wall, J s^{-1}m^{-2} K^{-1}
K_m = film mass transfer coefficient, m s^{-1}
$M1$ = molecular weight of components 1, g mol^{-1}
$M2$ = molecular weight of components 1, g mol^{-1}
P = pressure, Pa
P_i = partial pressure of component i, bar
q_i = adsorbed phase concentration of component i, mol kg^{-1}
q_i^* = adsorbed concentration of component i at equilibrium with the gas, mol kg^{-1}
R = ideal gas constant, J K^{-1} mol^{-1}
r_c = crystals/micropore radius, m
r_{pore} = macropores radius, m
R_p = particle radius, m
t = time, s
T = temperature of the gas phase, K
T_{hx} = temperature of the wall, K

https://dx.doi.org/10.1021/acs.iecr.9b06387
Ind. Eng. Chem. Res. 2020, 59, 7198−7211

T_s = temperature of the solid phase, K
u = superficial gas velocity, m s^{-1}
v_s = velocity of the solid phase, m s^{-1}
z = axial coordinate in the moving bed, m
Y_i = molar fraction of component i

GREEK SYMBOLS

ΔH_i^0 = isosteric heat of adsorption of component i, J mol^{-1}
ε_c = column void fraction
ε_p = particle porosity
λ = heat axial dispersion coefficient, J m^{-1} s^{-1} K^{-1}
λ_{pk} = heat axial dispersion coefficient of structured packing, J m^{-1} s^{-1} K^{-1}
ξ = volumetric fraction of structured packing
ρ_p = particle density, kg m^{-3}
ρ_{pk} = density of structured packing, kg m^{-3}
σ = Lennard-Jones parameter (collision diameter), Å
Ω = dimensionless collision integral of binary diffusivity

REFERENCES

(1) Eddaoudi, M.; Kim, J.; Rosi, N.; Vodak, D.; Wachter, J.; O'Keeffe, M.; Yaghi, O. M. Systematic design of pore size and functionality in isoreticular MOFs and their application in methane storage. *Science* **2002**, *295*, 469.
(2) Rosi, N. L.; Eckert, J.; Eddaoudi, M.; Vodak, D. T.; Kim, J.; O'Keeffe, M.; Yaghi, O. M. Hydrogen storage in microporous metal-organic frameworks. *Science* **2003**, *300*, 1127.
(3) Morris, R.; Wheatley, P. S. Gas storage in nanoporous materials. *Angew. Chem., Int. Ed.* **2008**, *47*, 4966.
(4) Sculley, J.; Yuan, D.; Zhou, H.-C. The current status of hydrogen storage in metal-organic frameworks-updated. *Energy Environ. Sci.* **2011**, *4*, 2721.
(5) Gangu, K. K.; Maddila, S.; Mukkamala, S. B.; Jonnalagadda, S. B. Characteristics of MOF, MWCNT and graphene containing materials for hydrogen storage: A review. *J. Energy Chem.* **2019**, *30*, 132.
(6) Makal, T. A.; Li, J.-R.; Lu, W.; Zhou, H.-C. Methane storage in advanced porous materials. *Chem. Soc. Rev.* **2012**, *41*, 7761.
(7) Peng, Y.; Krungleviciute, V.; Eryazici, I.; Hupp, J. T.; Farha, O. K.; Yildirim, T. Methane storage in metal-organic frameworks: Current records, surprise findings, and challenges. *J. Am. Chem. Soc.* **2013**, *135*, 11887.
(8) Mason, J. A.; Veenstra, M.; Long, J. R. Evaluating metal-organic frameworks for natural gas storage. *Chem. Sci.* **2014**, *5*, 32.
(9) Gomez-Gualdron, D. A.; Wilmer, C. E.; Farha, O. K.; Hupp, J. T.; Snurr, R. Q. Exploring the limits of methane storage and delivery in nanoporous materials. *J. Phys. Chem. C* **2014**, *118*, 6941.
(10) Shen, J.; Sulkowski, J.; Beckner, M.; Dailly, A. Effects of textural and surface characteristics of metal-organic frameworks on the methane adsorption for natural gas vehicular application. *Microporous Mesoporous Mater.* **2015**, *212*, 80.
(11) Bastin, L.; Barcia, P. S.; Hurtado, E. J.; Silva, J. A. C.; Rodrigues, A. E.; Chen, B. L. A microporous metal-organic framework for separation of CO2/N2 and CO2/CH4 by fixed-bed adsorption. *J. Phys. Chem. C* **2008**, *112*, 1575.
(12) Adil, K.; Belmabkhout, Y.; Pillai, R. S.; Cadiau, A.; Bhatt, P. M.; Assen, A. H.; Maurin, G.; Eddaoudi, M. Gas/vapour separation using ultra-microporous metal-organic frameworks: insight into the structure/separation relationship. *Chem. Soc. Rev.* **2017**, *46*, 3402.
(13) Ahmad, R.; Wong-Foy, A. G.; Matzger, A. J. Microporous coordination polymers as selective sorbents for liquid chromatography. *Langmuir* **2009**, *25*, 11977.
(14) Hindocha, S.; Poulston, S. Study of the scale-up, formulation, ageing and ammonia adsorption capacity of MIL-100(Fe), Cu-BTC and CPO-27(Ni) for use in respiratory protection filters. *Faraday Discuss.* **2017**, *201*, 113.
(15) de Lange, M. F.; Zeng, T.; Vlugt, T. J. H.; Gascon, J.; Kapteijn, F. Manufacture of dense CAU-10-H coatings for application in adsorptive driven heat pumps: optimization and characterization. *CrystEngComm* **2015**, *17*, 5911.
(16) Teo, H. W. B.; Chakraborty, A.; Kayal, S. Formic acid modulated (fam) aluminium fumarate MOF for improved isotherms and kinetics with water adsorption: Cooling/heat pump applications. *Microporous Mesoporous Mater.* **2018**, *272*, 109.
(17) Trapani, F.; Polyzoidis, A.; Loebbecke, S.; Piscopo, C. G. On the general water harvesting capability of metal-organic frameworks under well-defined climatic conditions. *Microporous Mesoporous Mater.* **2016**, *230*, 20.
(18) Quiros, J.; Boltes, K.; Aguado, S.; de Villoria, R. G.; Vilatela, J. J.; Rosal, R. Antimicrobial metal-organic frameworks incorporated into electrospun fibers. *Chem. Eng. J.* **2015**, *262*, 189.
(19) Jiao, L.; Wang, Y.; Jiang, H. L.; Xu, Q. Metal-organic frameworks as platforms for catalytic applications. *Adv. Mater.* **2018**, *30* (37), 1703663.
(20) Shekhah, O.; Liu, J.; Fischer, R. A.; Woll, C. MOF thin films: existing and future applications. *Chem. Soc. Rev.* **2011**, *40*, 1081.
(21) Stavila, V.; Talin, A. A.; Allendorf, M. D. MOF-based electronic and optoelectronic devices. *Chem. Soc. Rev.* **2014**, *43*, 5994.
(22) Wales, D. J.; Grand, J.; Ting, V. P.; Burke, R. D.; Edler, K. J.; Bowen, C. R.; Mintova, S.; Burrows, A. D. Gas sensing using porous materials for automotive applications. *Chem. Soc. Rev.* **2015**, *44*, 4290.
(23) Low, J. J.; Benin, A. I.; Jakubczak, P.; Abrahamian, J. F.; Faheem, S. A.; Willis, R. R. Virtual high throughput screening confirmed experimentally: porous coordination polymer hydration. *J. Am. Chem. Soc.* **2009**, *131* (43), 15834.
(24) Kusgens, P.; Zgaverdea, A.; Fritz, H. G.; Siegle, S.; Kaskel, S. Metal-organic frameworks in monolithic structures. *J. Am. Ceram. Soc.* **2010**, *93*, 2476.
(25) Tagliabue, M.; Rizzo, C.; Millini, R.; Dietzel, P. D. C.; Blom, R.; Zanardi, S. Methane storage on CPO-27-Ni pellets. *J. Porous Mater.* **2011**, *18*, 289.
(26) Hong, W. Y.; Perera, S. P.; Burrows, A. D. Manufacturing of metal-organic framework monolits and their application in CO2 adsorption. *Microporous Mesoporous Mater.* **2015**, *214*, 149.
(27) Dietzel, P. D. C.; Besikiotis, V.; Blom, R. Application of metal–organic frameworks with coordinatively unsaturated metal sites in storage and separation of methane and carbon dioxide. *J. Mater. Chem.* **2009**, *19*, 7362.
(28) Xiang, S.; He, Y.; Zhang, Z.; Wu, H.; Zhou, W.; Krishna, R.; Chen, B. Microporous metal-organic framework with potential for carbon dioxide capture at ambient conditions. *Nat. Commun.* **2012**, *3* (1), 954.
(29) Nugent, P.; Belmabkhout, Y.; Burd, S. D.; Cairns, A. J.; Luebke, R.; Forrest, K.; Pham, T.; Ma, S.; Space, B.; Wojtas, L.; Eddaoudi, M.; Zaworotko, M. J. Porous materials with optimal adsorption thermodynamics and kinetics for CO2 separation. *Nature* **2013**, *495*, 80.
(30) McDonald, T. M.; Mason, J. A.; Kong, X.; Bloch, E. D.; Gygi, D.; Dani, A.; Crocella, V.; Giordanino, F.; Odoh, S. O.; Drisdell, W. S.; Vlaisavljevich, B.; Dzubak, A. L.; Poloni, R.; Schnell, S. K.; Planas, N.; Lee, K.; Pascal, T.; Wan, L. F.; Prendergast, D.; Neaton, J. B.; Smit, B.; Kortright, J. B.; Gagliardi, L.; Bordiga, S.; Reimer, J. A.; Long, J. R. Cooperative insertion of CO_2 in diamine-appended metal-organic frameworks. *Nature* **2015**, *519* (7543), 303.
(31) Kizzie, A. C.; Wong-Foy, A. G.; Matzger, A. J. Effect of humidity on the performance of Microporous Coordination polymers as adsorbents for CO2 capture. *Langmuir* **2011**, *27* (10), 6368.
(32) Dasgupta, S.; Divekar, S.; Aarti; Spjelkavik, A. I.; Didriksen, T.; Nanoti, A.; Blom, R. Adsorption properties and performance of CPO-27-Ni/alginate spheres during multicycle pressure-vacuum-swing adsorption (PVSA) CO_2 capture in the presence of moisture. *Chem. Eng. Sci.* **2015**, *137*, 525.
(33) Masala, A.; Vitillo, J. G.; Mondino, G.; Grande, C. A.; Blom, R.; Manzoli, M.; Marshall, M.; Bordiga, S. CO_2 capture in dry and wet conditions in UTSA-16 metal-organic framework. *ACS Appl. Mater. Interfaces* **2017**, *9*, 455.

https://dx.doi.org/10.1021/acs.iecr.9b06387
Ind. Eng. Chem. Res. 2020, 59, 7198−7211

(34) Spjelkavik, A. I.; Aarti; Divekar, S.; Didriksen, T.; Blom, R. Forming MOFs into spheres by use of molecular gastronomy methods. *Chem. - Eur. J.* **2014**, *20*, 8973−8978.
(35) Berg, C. Hypersorption process for separation of light gases. *Trans. AIChE* **1946**, *XLII*, 665.
(36) Grande, C. A.; Kvamsdal, H.; Mondino, G.; Blom, R. Development of moving bed temperature swing adsorption (MBTSA) process for post-combustion CO_2 capture: Initial benchmarking in a NGCC context. *Energy Procedia* **2017**, *114*, 2203.
(37) Mondino, G.; Grande, C. A.; Blom, R. Effect of gas recycling on the performance of a moving bed temperature swing (MBTSA) process for CO_2 capture in a coal fired power plant context. *Energies* **2017**, *10*, 745.
(38) Mondino, G.; Grande, C. A.; Blom, R.; Nord, L. O. Moving bed temperature swing adsorption for CO2 capture from a natural gas combined cycle power plant. *Int. J. Greenhouse Gas Control* **2019**, *85*, 58.
(39) Krishnamurthy, S.; Blom, R.; Ferrari, M. C.; Brandani, S. Adsorption and diffusion of CO2 in CPO-27−Ni beads. *Adsorption* **2019**, DOI: 10.1007/s10450-019-00162-x.
(40) Dietzel, P. D. C.; Panella, B.; Hirscher, M.; Blom, R.; Fjellvag, H. Hydrogen adsorption in a nickel based coordination polymer with open metal sites in the cylindrical cavities of the desolvated framework. *Chem. Commun.* **2006**, *9*, 959.
(41) Lopes, F. V.; Grande, C. A.; Ribeiro, A. M.; Oliveira, E. L.; Loureiro, J. M.; Rodrigues, A. E. Enhancing capacity of activated carbons for hydrogen purification. *Ind. Eng. Chem. Res.* **2009**, *48*, 3978.
(42) Grande, C. A.; Lopes, F. V.; Ribeiro, A. M.; Loureiro, J. M.; Rodrigues, A. E. Adsorption of Off-Gases from Steam Methane Reforming (H_2, CO_2, CH_4, CO and N_2) on Activated Carbon. *Sep. Sci. Technol.* **2008**, *43*, 1338.
(43) *Scilab*, version 6.0.2; Scilab Enterprises, 2019. http://www.scilab.org (accessed April 2020).
(44) Taqvi, S. M.; LeVan, M. D. Virial description of two-component adsorption on homogeneous and heterogeneous surfaces. *Ind. Eng. Chem. Res.* **1997**, *36*, 2197.
(45) *gPROMS Model Builder*, version 5.0; Process System Enterprise (PSE), 2017.
(46) Liu, Z.; Grande, C. A.; Li, P.; Yu, J.; Rodrigues, A. E. Multi-bed Vacuum Pressure Swing Adsorption for carbon dioxide capture from flue gas. *Sep. Purif. Technol.* **2011**, *81*, 307.
(47) *Thermoflow package*, version 27.0; Thermoflow, Inc., 2017.
(48) Elsayed, E.; Al-Dadah, R.; Mahmoud, S.; Anderson, P. A.; Elsayed, A.; Youssef, P. G. CPO-27(Ni), aluminium fumarate and MIL-101(Cr) MOF materials for adsorption water desalination. *Desalination* **2017**, *406*, 25−36.
(49) Friedrich, D.; Mangano, E.; Brandani, S. Automatic estimation of kinetic and isotherm parameters from ZLC experiments. *Chem. Eng. Sci.* **2015**, *126*, 616−624.
(50) Lee, D. W.; Didriksen, T.; Olsbye, U.; Blom, R.; Grande, C. A. Shaping of metal-organic framework UiO-66 using alginates: effect of operation variables. *Sep. Purif. Technol.* **2020**, *235*, 116182.
(51) Queen, W. L.; Hudson, M. R.; Bloch, E. D.; Mason, J. A.; Gonzalez, M. I.; Lee, J. S.; Gygi, D.; Howe, J. D.; Lee, K.; Darwish, T. A.; James, M.; Peterson, V. K.; Teat, S. J.; Smit, B.; Neaton, J. B.; Long, J. R.; Brown, C. M. Comprehensive study of carbon dioxide adsorption in the metal-organic frameworks M2(dobdc) (M= Mg, Mn, Fe, Co, Ni, Cu, Zn). *Chem. Sci.* **2014**, *5*, 4569−4581.
(52) Hu, X.; Brandani, S.; Benin, A. I.; Willis, R. R. Development of a semiautomated zero length column technique for carbon capture applications: study of diffusion behavior of CO_2 in MOFs. *Ind. Eng. Chem. Res.* **2015**, *54*, 5777.
(53) Liu, J.; Wang, Y.; Benin, A. I.; Jakubczak, P.; Willis, R. R.; LeVan, M. D. CO_2/H_2O adsorption equilibrium and rates on metal−organic frameworks: HKUST-1 and Ni/DOBDC. *Langmuir* **2010**, *26*, 14301.
(54) Brandani, F.; Ruthven, D. M.; Coe, C. G. Measurement of Adsorption Equilibrium by the Zero Length Column (ZLC) Technique Part 1: Single-Component Systems. *Ind. Eng. Chem. Res.* **2003**, *42*, 1451−1461.
(55) Rajagopalan, A. K.; Avila, A. M.; Rajendran, A. Do adsorbent screening metrics predict process performance? A process optimization based study for post-combustion capture of CO_2, *Int. Int. J. Greenhouse Gas Control* **2016**, *46*, 76−85.
(56) *MATLAB*, version 9.7; The MathWorks, Inc., 2019.
(57) Hu, X.; Mangano, E.; Friedrich, D.; Ahn, H.; Brandani, S. Diffusion mechanism of CO_2 in 13X zeolite beads. *Adsorption* **2014**, *20*, 121.

https://dx.doi.org/10.1021/acs.iecr.9b06387
Ind. Eng. Chem. Res. 2020, 59, 7198−7211